Anderson localization of ultrasound in three dimensions

J. H. Page

Department of Physics and Astronomy
University of Manitoba
Winnipeg, MB Canada R3T 2N2

Summary. — Some fifty years after Anderson localization was first proposed, there is currently a resurgence of interest in this phenomenon, which has remained one of the most challenging and fascinating aspects of wave transport in random media. This paper summarizes recent progress in demonstrating the localization of ultrasound in a "mesoglass" made by assembling aluminum beads into a disordered three-dimensional elastic network. In this system, the disorder is sufficiently strong that interference leads to trapping of the waves at intermediate frequencies, as demonstrated by studying three different fundamental aspects of Anderson localization: time-dependent transmission, transverse confinement of the waves, and the statistics of the non-Gaussian intensity fluctuations. Additional ultrasonic experiments have been performed to reveal the multifractal character of the wave functions near the Anderson transition. This is the first time that so many different aspects of localization have been studied simultaneously, providing very convincing evidence for the localization of ultrasonic waves in the presence of disorder in three dimensions, and enabling new aspects of Anderson localization to be studied experimentally.

(*) Published in the Proceedings of the International School of Physics Enrico Fermi,

1. – Introduction

During the 1980s, it was realized that Anderson localization [1, 2] - the spatial trapping of waves due to disorder - is not only a quantum effect, but is, more generally, a phenomenon that may occur for any type of wave: quantum or classical. This phenomenon results from the interference of waves that have been multiply scattered in a disordered medium, and therefore should be observable so long as the disorder is sufficiently strong and coherence is maintained, the latter condition being readily satisfied for classical waves such as light, microwaves, sound, elastic waves, and even seismic waves. To appreciate the analogy that exists between quantum and classical wave behaviour in disordered media, one need go no further than to compare the Schrodinger and Helmholtz equations in the presence of disorder, as is outlined in appendix A. This comparison shows that these equations for quantum and classical waves have the same form, but with an important difference. This difference implies that it is only possible to localize classical waves at intermediate frequencies where the wavelength is comparable to the size of the scattering inhomogeneities, and not more or less trivially at very low frequencies, as in the case for electrons. This absence of "bound states" for classical waves, and the need to achieve sufficiently strong scattering, makes the localization of classical waves challenging to observe in practice.

Not withstanding these challenges, there are several reasons why classical waves are potentially better adapted to observing the phenomenon of Anderson localization directly. For electrons or other quantum particles (e.g., cold atoms), experiments must be performed at low temperatures to minimize the effects of inelastic scattering, which destroys phase coherence. There is no such restriction for classical waves. Classical waves also have the advantage that the analogue of electron-electron interactions (nonlinearities) can be avoided by suitable choices of materials and power levels. Perhaps most significant is the versatility of experiments with classical waves, where measurements as a function of both time and space are feasible, potentially yielding much more information about localization than is possible by simply measuring the total transmittance at a single frequency. The latter is equivalent to measuring the overall sample conductance for electronic systems, the technique that has been used almost exclusively in studies of electron localization.

Once these advantages of classical waves were appreciated, experimental work showing strong localization of both acoustic and electromagnetic waves followed in one- and two-dimensional systems (1D and 2D), as well as in quasi-1D waveguides [3, 4, 5, 6, 7, 8]. These were significant steps forward, as they permitted localized wave functions and their statistical properties to be studied directly, stimulating many new theoretical advances as well. However, the central question in the field, whether or not classical waves

Course CLXXIII, "Nano Optics and Atomics: Transport of Light and Matter Waves", edited by R. Kaiser, D.S. Weirsma and L. Fallani (IOS, Amsterdam; SIF, Bologna, 2011) pp. 95-114. The original publication is available from SIF at http://www.sif.it/SIF/en/portal/books/series/rendiconti_fermi.

could be localized in *three* dimensions (3D), has been more difficult to answer, despite several *tour-de-force* experiments in optics [9, 10, 11]. Three dimensions is especially important, as it is only in 3D that scaling theory predicts the existence of a real transition from propagating to localized modes [12]. In seeking experimental evidence, one of the problems, in addition to the challenges mentioned above, has been absorption, which is always present to some extent for classical waves, and which leads to a reduction in total transmission having the same dependence on sample thickness as localization. Thus, to demonstrate 3D localization convincingly, it is necessary to combine a number of experimental approaches that can probe key signatures of localization: e.g., anomalous dynamics (time dependence), spatial confinement of the waves, and the statistics of the large intensity fluctuations.

This paper describes the recent progress that has been achieved using ultrasonic experiments, in combination with advances in the self-consistent theory of localization, to unambiguously demonstrate Anderson localization in three dimensions [13]. One key to this success has been the construction of sufficiently strongly scattering samples, which are described in the next section (section **2**). The following sections outline the three main experimental approaches that have been exploited to obtain evidence of localization: time dependent transmission (section **3**), transverse confinement (section **4**) and statistics (section **5**). This last section ends with an example of an aspect of localization in 3D that has not been accessible to experimental study previously, namely the structure of localized wave functions as characterized by their multifractal properties [14].

2. – Mesoglasses: porous elastic solids with very strong scattering

In samples suitable for localization experiments, it is generally important to maximize the scattering strength and minimize the absorption (or dissipation). Despite the very large scattering contrast between solids and liquids for ultrasonic waves, with differences in acoustic impedance as large as 10 to 60 being readily achievable, suspensions of solid spherical particles in a fluid, as described in [15], were found to have insufficiently strong scattering. This is true even in the intermediate frequency regime, where the wavelength is comparable to the size of the scatterers and shape resonances can enhance the scattering. The other problem with such samples is the relatively large dissipation, one important contribution being viscous losses at the interface between the solid and liquid phases. To avoid this difficulty, we decided to take a different approach and investigate porous, single-component solid systems instead. Our initial experiments were performed on highly porous solid networks of well-sintered glass beads, revealing interesting plateaus in both the diffusion coefficient and the density of states [16]. However, in spite of very strong scattering, no evidence of localization was seen in these early experiments. To make better samples for observing Anderson localization, three important steps were taken: the glass particles were replaced by aluminum, thereby further reducing the intrinsic absorption in the constituent particles; the particle radius a was increased, allowing higher effective frequencies (ka) to be accessed using the same ultrasonic transducers; and a new way was developed for joining the particles together into

Fig. 1. – One of the samples in which the localization of ultrasonic waves was observed in the intermediate frequency regime. The aluminum beads are brazed together with weak elastic links to form a disordered solid network, in which the ultrasonic waves become trapped after strong multiple scattering from the pores.

a solid network, allowing for better control of the interparticle contacts, and hence the scattering strength. In this way, a disordered elastic network of aluminum beads was created by brazing the beads together to form weak elastic bonds between the beads while preserving their spherical shape, as shown in Fig. 1. Such a structure may be viewed as a "mesoglass" in which the beads are linked by narrow necks to form a disordered material with mesoscopic particles as the building blocks rather than atoms, and with elastic bonds between the particles rather than interatomic forces. The beads were monodisperse, with a diameter of 4.11 ± 0.03 mm, and the samples had an aluminum volume fraction of approximately 55%, corresponding to random loose packing of the beads before brazing. The samples were slab-shaped, with circular cross sections of diameter much larger than the thickness L, which ranged from 8 mm to 23 mm.

To study the samples using ultrasonic immersion techniques [15, 17], the samples were first waterproofed with very thin plastic walls, so that the samples remained dry when immersed in a water tank between the generating and detecting transducers. This procedure ensured that wave transport occurred through the aluminum network, where the incident acoustic wave from the water (longitudinal polarization only) was converted into an elastic wave in the solid (which supports both longitudinal and transverse polarizations). Measurements were performed over a wide frequency range from 100 kHz to several MHz, since this corresponds to the intermediate frequency regime for this structure, where the wavelength is comparable to the bead and pore sizes and very strong scattering is expected. Initial characterization of the samples was performed by measuring the amplitude transmission coefficient, obtained from the ratio of the fast Fourier transforms of the transmitted and input signals. These measurements confirmed the existence band gaps in this type of system, as first reported by Turner and Weaver in

1998 [18]. The gaps occur because the coupled resonances of the aluminum beads broaden to form pass bands, with band gaps forming in between; wide band gaps are observed so long as the coupling is not too strong, which is the case for our samples. For some of the samples, it was possible to extract the coherent ballistic pulse and measure the longitudinal phase and group velocities v_p and v_g, as well as the scattering mean free path l. Very strong scattering was demonstrated by the observation that, outside the band gaps, the product of wave vector and mean free path varied from nearly 1 to 2.5 over this frequency range, thus approaching the Ioffe-Regel limit $kl = 1$. Although we were not able to measure kl for transverse waves in these experiments, previous experiments on sintered glass bead networks have shown similar values of kl for both transverse and longitudinal waves in the strong scattering regime [19]. Localization is expected when $kl \lesssim 1$, but the exact critical value kl_c at which the transition occurs is not known [20], and is likely to be wave and sample dependent; thus, these initial measurements suggest that localization of ultrasonic waves may indeed be possible in these samples.

3. – Time-dependent Transmission

Our first experiment to investigate wave transport by multiply scattered waves in these samples was performed using a short quasi-planar incident pulse and measuring the time-dependent transmitted field with a miniature hydrophone. The hydrophone was scanned over a square 55x55 grid parallel to, and within a few wavelengths of, the sample surface. The grid separation was typically equal to the wavelength in water (for more details on the method, see [15] and [17]). A schematic diagram of the setup is shown in fig. 2(a). Several representative waveforms measured at different positions in the speckle pattern are shown in fig. 2(b); this example was recorded for a two-cycle input pulse with a central frequency of 0.25 MHz, showing that data for a long range of propagation times, corresponding to progressively longer and longer multiple scattering paths, is observable in these samples. Before determining the time-dependent intensity $I(t)$, the waveforms were digitally filtered to limit the bandwidth to 5% of the central frequency of the pulse. The average transmitted intensity $I(t)$ was then determined by squaring the envelope of the field at each position, averaging over each position in the speckle pattern, and normalizing by the peak of the input pulse. Typical time-dependent intensity profiles are shown in figs. 2(c) and (d), revealing the excellent signal-to-noise and large dynamic range obtained at both low and high frequencies in the range of interest between 0.1 and 3 MHz.

Note that, even though both compressional (longitudinally polarized) and shear (transversely polarized) waves are excited in these elastic materials, in which shear waves typically propagate at roughly half the speed of longitudinal waves, a single intensity profile $I(t)$ is seen at all frequencies. This occurs because the polarizations mix at each scattering event. Thus, after only a few scatterings, the total energy density becomes equipartitioned between compressive and shear waves [21, 22, 23], according to their respective energy densities U_L and U_T. For weak disorder,

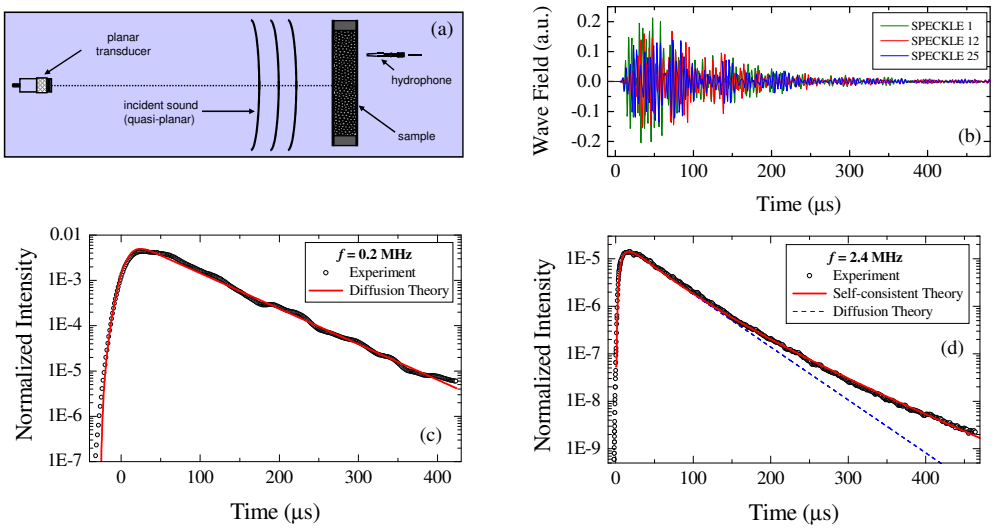

Fig. 2. – (a) Schematic diagram indicating the experimental setup for measuring the time-dependent transmission. (b) The transmitted field measured by the hydrophone at three different positions near the sample surface. The source was a short two-cycle pulse with a central frequency of 0.25 MHz. The peak of the input pulse occurs at $t = 0$. (c) Transmitted intensity $I(t)$ at a representative frequency of 0.2 MHz in the diffuse regime for a sample with thickness $L = 14.5$ mm. The best fit to diffusion theory (solid red curve) with $R = 0.85$ yields $D = 3.0$ mm/μs and $l^* = 2.5$ mm, with τ_a being to large to be measurable. (d) $I(t)$ for the same sample at a frequency of 2.4 MHz in the localized regime. The data cannot be fitted by diffusion theory (dashed blue curve), but is well fitted by the self-consistent theory of localization (solid red curve) with $\xi = 15$ mm, $l_B^* = 2$ mm, $D_B = 16$ mm$^2/\mu$s and $\tau_a = 160$ μs.

$$U_L(\omega) \propto \rho_L(\omega) = \frac{k^2}{2\pi^2}\frac{dk}{d\omega} \propto \frac{\omega^2}{v_{p,L}^2 v_{g,L}} \tag{1}$$

$$U_T(\omega) \propto \frac{2\omega^2}{v_{p,T}^2 v_{g,T}} \tag{2}$$

Since the energy density depends on the inverse of the cube of the wave speeds, transverse waves dominate the energy transport. At sufficiently low frequencies, one one might expect that the transport is diffusive and that there are no renormalization effects due to interference, so that the Boltzmann diffusion coefficient $D_B = v_E l_B^*/3$ and transport mean free path l_B^* are observed. In this regime, providing that the scattering is isotropic ($l = l^*$) and the energy velocity is equal to the group velocity, a simple relation can be derived for the effective energy-density-weighted average diffusion coefficient:

$$D = \frac{1}{3}\left(\frac{l_L^*}{v_{p,L}^2} + \frac{2l_T^*}{v_{p,T}^2}\right) \Bigg/ \left(\frac{1}{v_{p,L}^2 v_{g,L}} + \frac{2}{v_{p,T}^2 v_{g,T}}\right) = \frac{1}{3} v_E l^* \tag{3}$$

Here, the effective transport mean free path being given by

$$l^* = \left(\frac{l_L^*}{v_{p,L}^2} + \frac{2l_T^*}{v_{p,T}^2}\right) \Bigg/ \left(\frac{1}{v_{p,L}^2} + \frac{2}{v_{p,T}^2}\right) \tag{4}$$

and the effective energy velocity by

$$v_E = \left(\frac{1}{v_{p,L}^2} + \frac{2}{v_{p,T}^2}\right) \Bigg/ \left(\frac{1}{v_{p,L}^2 v_{g,L}} + \frac{2}{v_{p,T}^2 v_{g,T}}\right). \tag{5}$$

While the general case is more complex, these relations give some insight into the consequences of energy equipartition, and provide a simple starting point for comparing data with the predictions of the diffusion approximation whenever the ballistic parameters can be measured.

For our brazed aluminum bead samples, the ultrasonic wave transport was indeed found to be diffusive at low frequencies. The evidence for diffusive transport can be seen in the exponential decay of the ensemble-averaged transmitted intensity at long times, $I(t) \propto \exp(-t/\tau_D)$, which was observed for frequencies up to 0.4 MHz. In this frequency range, the entire time dependence of $I(t)$ is well described by diffusion theory, as is illustrated in fig. 2(c), which compares diffusion theory with data measured at 0.2 MHz. By fitting theory to experiment, the diffusion coefficient was determined, and the transport mean free path was estimated from the dependence of the transmitted intensity on boundary conditions. One consequence of the equipartition of elastic energy inside the sample is that the internal reflection coefficient R is large, as the outside medium only supports longitudinal waves; nonetheless R can still be reliably determined from the measured ballistic parameters by accounting for the angle-dependent reflection coefficients for all polarizations [24], thereby reducing the number of fitting parameters. In this frequency range, D was found to be roughly independent of frequency, consistent with earlier experiments on sintered glass bead networks [16]. Significantly, we found that absorption, which attenuates $I(t)$ by the factor $\exp(-t/\tau_a)$, where τ_a is the absorption time, was too small to measure in this frequency range, consistent with our expectations that absorbtion would be much much lower for these samples than in most strongly scattering acoustic systems, such as suspensions of particles in a fluid [17]. The success in interpreting these data using diffusion theory establishes that multiply scattered ultrasound propagates diffusively in the lower part of the intermediate frequency range, which is the diffusive regime for this system.

In the upper part of the intermediate frequency range ($\sim$ 2 MHz), the time dependence of $I(t)$ shows qualitatively different behavior: at long times, $I(t)$ decays more slowly than in the diffusive regime, with a non-exponential tail that cannot be explained by the diffusion approximation (fig. 2(d)). This behavior has been viewed as a slowing down of the effective diffusion coefficient $D(t)$ with propagation time, reflecting a time-dependent renormalization of D due to interference effects associated with localization [7, 10]. Physically, the waves become trapped by the disorder, but eventually manage to escape from the sample, suggesting that Anderson localization may be occurring in these samples. To interpret these data quantitatively, we exploit recent progress in the self-consistent theory of localization, initially developed for electron localization by Vollhardt and Wölfle in 1980 [25, 26]. The basic idea in this theory is to described the renormalization of the diffusion coefficient by accounting for constructive interferences between reciprocal paths, which lead to an increased probability that a quantum particle or classical wave returns to the same spot. The recent progress [27, 28] enables the dynamics of wave transport to be predicted for experiments such as ours, which involve *open* three-dimensional systems. The new aspect of this theory is the incorporation of boundary conditions self-consistently, thereby accounting for the fact that the return probability is less reduced near the boundaries, where the wave may escape, so that the renormalization of D by interference is less there. This leads to a position-dependent dynamic diffusivity kernel $D(\vec{r}, t-t')$. The solid curve in fig. 2(d) is a fit of the self-consistent theory to our data at 2.4 MHz, and gives an excellent description of the experiment at all propagation times. From this fit, we are able to determine the localization length $\xi = 15$ mm for this sample. This measurement of ξ is feasible since several key parameters (l and v_p, and hence kl and R) are known for our sample from independent ballistic measurements, leaving the localization length, the bare transport mean free path l_B^*, the diffusion time τ_D , and the absorption time τ_a as fitting parameters. In the self-consistent theory, the localization length is related the ratio of kl to its critical value at the mobility edge, $\chi = kl/(kl)_c$, by $\xi/l_B^* = [6/(kl_B^*)_c^2]\chi^2/(1-\chi^4)$. Thus ξ is positive in the localization regime where $\chi < 1$, and negative in the diffuse regime, where the absolute value of ξ plays the role of a correlation length in the vicinity of a phase transition. The most important points to emerge from the fitting are not only that the self-consistent theory describes the time dependence of the measured $I(t)$ very well, but also that it is only possible to fit to the experimental measurements with the theory when $\xi > 0$. This gives strong evidence for the dynamic localization of ultrasound in our sintered aluminum bead system.

4. – Transverse Confinement

The measurements of the time-dependent transmission described in the previous section give only indirect evidence of Anderson localization. Is it possible to observe localization more directly? To answer this question, the quasi-plane wave source was replaced by a point source (approximately a wavelength wide), and the transmitted intensity was measured as a function of both position and time on the opposite face of the sample. The point source was obtained by focusing the input pulse through a narrow aperture onto

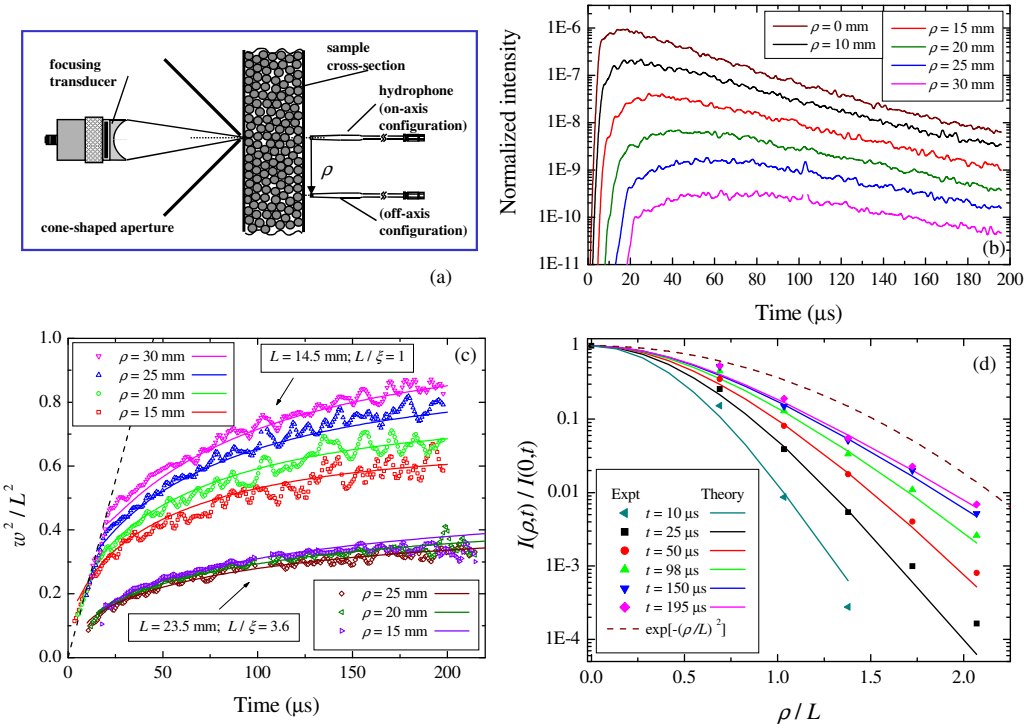

Fig. 3. – (a) Schematic illustration (not to scale) of the setup for measuring the dynamic transverse confinement of the transmitted intensity emitted by a point source in the localization regime. (b) Average time- and position- dependent intensity, $I(\rho, t)$ at several positions ρ for the setup shown in (a). The frequency (2.4 MHz) and sample are the same as in fig. 2(d). (c) Mean square width $w_\rho^2(t)$ of the intensity ratio $I(\rho, t)/I(0, t)$ as a function of time for the data shown in (b) and for a second sample with a thickness $L = 23.5$ mm. The frequency is 2.4 MHz for both samples. The solid curves are the best fits of the self-consistent theory to the experimental data (symbols) with $l_B^* = 2$ mm, $D_B = 11$ mm$^2/\mu$s, $\xi = 15$ mm for the $L = 14.5$ mm sample, and $\xi = 7$ mm for the $L = 23.5$ mm sample. Other parameters used in the calculations, $kl = 1.8$ and $R = 0.82$, were determined from independent ballistic measurements. The dashed line shows the linear time-dependence of w^2 that would occur for diffuse waves, using a value for D of 1.25 mm$^2/\mu$s. (d) Dependence of the intensity ratio on distance ρ at selected times, showing the non-Gaussian profile that is found both experimentally (symbols) and theoretically (solid curves).

the sample surface at the point $\rho = 0$, as shown schematically in fig. 3(a). The transmitted wave field was measured with subwavelength resolution using a hydrophone, which was moved over a range of transverse positions ρ for a given position of the source. The transmitted intensity $I(\rho, t)$ was calculated from the measured field as indicated in the previous section. To average the intensity for each ρ and t over a large number (typically $55^2 = 3025$) of speckle spots, the position of the sample was scanned in the $x - y$ plane parallel to the surface of the sample. Typical data for $I(\rho, t)$ at 2.4 MHz, measured on

the same sample for which $I(t)$ is reported in fig. 2, are shown in fig. 3(b). As expected, data for larger ρ start later because the distance from the source is greater; what was not expected is that the curves for different ρ decay at essentially the same rate at long times, i.e., they differ by a time-independent factor at long times. To understand this behaviour, the crucial quantity is the ratio $I(\rho,t)/I(0,t)$, which probes the dynamic spreading of the intensity profile in a plane parallel to the surface of the sample. Most importantly, this ratio is *independent of absorption*, since at each time, the absorption factor $\exp(-t/\tau_a)$ is the same for any ρ and therefore cancels in the ratio. We characterize this dynamic spatial profile of the intensity by its width $w_\rho(t)$, defined by $I(\rho,t)/I(0,t) = \exp(-\rho^2/w_\rho^2(t))$. As shown in ref. [15], $w_\rho^2(t) = 4Dt \propto t$ in the diffuse regime, providing an accurate method for measuring D that is independent of absorption and boundary conditions. By contrast, in the localized regime, the transverse width $w_\rho(t)$ exhibits completely different behaviour, shown in fig. 3(c) for two samples of different thickness. Instead of increasing linearly with propagation time, $w_\rho^2(t)$ saturates, approaching a constant value for each ρ at long times. Furthermore, the transverse spatial profile of the intensity is no longer Gaussian in the localized regime, since $w_\rho^2(t)$ depends on ρ - another clear departure from diffuse behaviour that is especially evident in the thinner sample. These results indicate that the data cannot be explained by assuming a diffusion coefficient $D(t)$ that depends only on time, since in this case the magnitude of $w(t) \sim \int D(t)dt$ would be independent of ρ [29]. The observed non-Gaussian shape of the spatial profiles is shown explicitly in fig. 3(d) for a range of times separated by (almost) equal intervals at long times, but by narrower intervals at early times. These data were measured on the thinner sample. A Gaussian curve with width equal to the sample thickness (dashed curve) is also included in this figure for comparison. Both figs. 3(c) and (d) show that the intensity profile initially grows with time, but then converges to a constant profile at long times, revealing how the initial propagation of the waves away from the source is brought to a halt by localization. This is exactly what is meant by localization. These data are therefore a very direct demonstration of 3D Anderson localization, and are, to the best of our knowledge, the most direct observations of this phenomenon to date.

Additional information about Anderson localization in these samples can be obtained by comparing the data with the predictions of the self-consistent theory. The solid curves in fig. 3(c) demonstrate that the behaviour of the dynamic transverse width is accurately predicted by the self-consistent theory, which gives an excellent fit to the data for all t and ρ, with a single set of parameters for each sample. The fits give $\xi = 15$ mm for the thinner sample ($L = 14.5$ mm – the same sample whose the time dependent transmission is plotted in fig. 2), and $\xi = 7$ mm for the thicker sample ($L = 23.5$ mm). These results suggest that the scattering is stronger in the thicker sample due to small differences in microstructure, showing that ξ is very sensitive to the degree of disorder, quantified by kl, near the localization threshold, as theory predicts. It is worth emphasizing explicitly that the non-Gaussian character of the experimental intensity profiles is quantitatively described by the self-consistent theory, showing the importance of accounting for the position dependence of D in the theory. These measurements of the localization length at 2.4 MHz enable us to estimate the proximity to the mobility edge $(kl)_c$, with kl being

only 1% below $(kl)_c$ at this frequency.

Compared with the plane wave case 2(d), these fits of the self-consistent theory for $w_\rho^2(t)$ provide a more accurate determination of the localization length. One reason is the elimination of absorption, so there is one less parameter to fit. In addition, the self-consistent theory predicts that the transverse width at long times depends predominantly on both the localization length ξ and sample thickness L, and since it is straightforward to measure L, the measurement of $w_\rho^2(t)$ provides a more direct way of determining ξ. For thick samples ($L >> \xi$), the width is no longer influenced by ρ, i.e., the statistical profile is again Gaussian, and the dependence of w^2 at long times on L and ξ has been shown to have a simple scaling form [31]: $w^2(t \to \infty) \approx 2L\xi(1 - \xi/L)$; thus, to leading order, the long time limit of w^2 is simply $2L\xi$.

One of the interesting predictions of the theory is a strong and rapid renormalization of the effective diffusion coefficient. As a result, D_B cannot be measured directly even at the earliest times at which transmission measurements can be made. The best fits give surprisingly large values of D_B, which imply $v_E > v_p$. Further theoretical work is needed to understand these apparently very large values of the energy velocity in the localized regime.

As the frequency is lowered, the transverse width increases, as is shown in fig. 4. One would expect that in the localized regime, the width $w_\rho(t)$ will always saturate at long times, whereas in the diffuse regime, the width will continue to grow with time as the energy density continues to expand in the transverse direction, albeit slowly near the mobility edge. These expectations are confirmed by the self-consistent theory, where recent calculations for thick samples show that the asymptotic value of $w^2(t)$ as $t \to \infty$ remains finite not only in the localized regime but even at the mobility edge, where the saturation value is approximately equal to the thickness of the sample, $w_\infty \approx L$ [31]. The experimental results plotted in fig. 4 appear consistent with these predictions. At the lowest frequency shown (0.7 MHz), the width clearly continues to increase without limit, and its increase is almost linear, indicating that at this frequency, the transport is subdiffusive. At 1.0 MHz, $w_\rho^2(t)/L^2$ remains less than 1 throughout the range of times where the signal could be measured, but is still increasing at the longest times, suggesting that this frequency is very close to, but on the diffusive side of, the critical value f_c at the mobility edge. At higher frequencies, $w_\rho^2(t)/L^2$ remains well below 1, and clearly saturates at long times for frequencies above 1.8 MHz, indicating that localization has set in. These results illustrate the behaviour of the transverse width in the vicinity of the Anderson transition, suggesting that it should be possible to use transverse confinement to measure the variation of the localization length as the mobility edge is approached. Work is currently in progress to examine this behaviour in detail.

Another interesting question concerns the time dependence of the transverse width, especially at early times where it characterizes the initial growth of the spatial intensity profile. In the localized regime, one might anticipate that the intensity would spread out from the source at a slower rate than for diffuse waves; does this imply that $w_\rho^2(t)$ still increases as a power law, with a smaller exponent than in the diffuse regime, or is the behaviour more complex? To examine possible power-law behaviour more closely, the

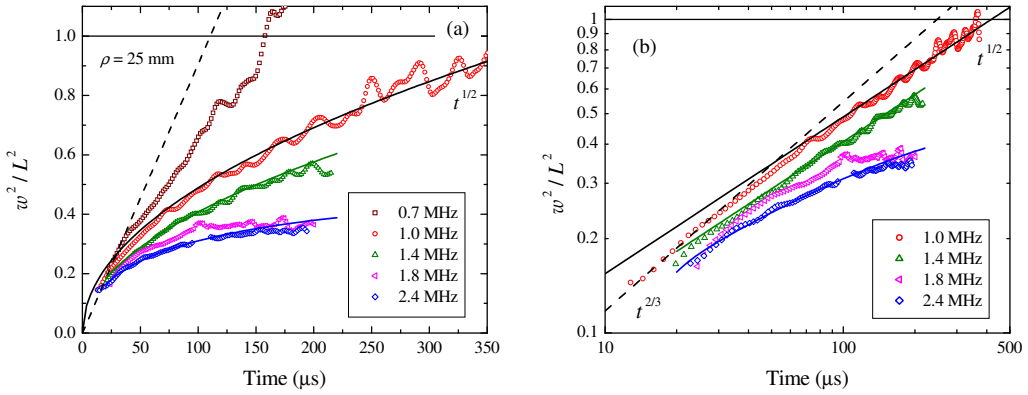

Fig. 4. – (a) Time dependence of the transverse width for several frequencies in the strong scattering regime, showing that the width increases as the frequency is lowered. The mean square width is normalized by the sample thickness squared ($L = 23.5$ mm for these data). The data are plotted for $\rho = 25$ mm, but the dependence on ρ is not large for this thick sample (see fig. 3). A mobility edge can be inferred to lie at a frequency between 1 and 1.8 MHz for this sample. (b) The same data plotted on doubly logarithmic scales to display the power-law behaviour of the time dependence near the mobility edge. At 1.0 MHz, the data are consistent with a crossover from $t^{2/3}$ to $t^{1/2}$ behaviour, as predicted by the dynamic self-consistent theory of localization.

experimental results for $w_\rho^2(t)/L^2$ are replotted in a doubly logarithmic scale in fig. 4(b). This figure shows that such behaviour is exhibited at 1.0 MHz near the mobility edge, but that there appear to be *two* power-law regimes. The data are consistent with an initial growth of $w_\rho(t)^2/L^2$ as $t^{2/3}$, followed by a slower $t^{1/2}$ regime, which at this frequency extends up to the maximum time at which signals could be recorded reliably. A $t^{1/2}$ regime is also seen over a smaller range of times ($\sim$ half a decade) at 1.4 MHz, before $w_\rho^2(t)/L^2$ starts to level off towards a constant value (the long-time data are not plotted here because the signal-to-noise ratio is poor at these times, preventing an accurate measurement of how the width levels off, although it is nonetheless clear that it drops below the $t^{1/2}$ curve for times $t > 220$ μs). These power laws have been predicted by the self-consistent theory for the initial expansion of the intensity from a point source located deep inside a thick sample ($L >> l$) [31], where a relatively simple estimate of the return probability may be obtained by neglecting the position dependence of D. By solving for $D(\Omega)$ at the mobility edge, Cherroret *et al.* show that the mean square radius of the 3D intensity profile grows as $t^{2/3}$ at short times ($t << L^2/D_B$), and as $t^{1/2}$ at longer times ($t >> L^2/D_B$) [31]. Assuming that the mean square transverse width for a slab sample scales with time in a similar way near the mobility edge, this provides a qualitative explanation of the time dependence seen in their numerical calculations [31] and in our experimental results (fig. 4). However, this simple argument for the initial time dependence of $w^2(t)$ does not explain the saturation at longer times.

To end this section, it is worth emphasizing again that these measurements of the

dynamic transverse confinement of the intensity due to localization are independent of absorption, which has been a major obstacle to reaching definitive conclusions in previous experiments [6, 9, 10, 11, 32]. The method provides a direct way of observing the trapping of waves by disorder. The behaviour revealed in figs. 3(c) and (d) is both qualitatively and quantitatively different to that seen for diffusive waves, and provides unambiguous evidence for the localization of ultrasound in these 3D samples.

5. – Statistical Approach to Localization

The previous sections have examined the marked changes that occur in the temporal and spatial profiles of the *average* intensity in the localized regime. Localization also leads to very large fluctuations in the transmitted intensity, and the measurement and analysis of their statistical properties can be used to reveal other signatures of localization [6]. To investigate this statistical approach to localization, we have measured the large spatial fluctuations of the intensity that occur in ultrasonic speckle patterns [13]. These were measured by scanning the hydrophone in a plane near the surface of the samples when illuminated on the opposite side with short pulse having a spatial profile that corresponds quite closely to a broad Gaussian beam. By taking the Fourier transform of the measured variations in the transmitted field, $\psi(x, y, t)$, the variation of the intensity $I(x, y)$ at each frequency in the bandwidth of the incident pulse was determined, enabling the near-field speckle patterns to be plotted, as illustrated in figs. 5(a) and (b) for frequencies in the diffuse and localized regimes, respectively. Even by eye, a clear difference can be seen between these two cases. In the diffuse regime, the speckles overlap and the overall fluctuations are less. By contrast, localized speckle patterns are characterized by a few very intense peaks, which are well separated from each other, so that the fluctuations across the speckle pattern are very much larger.

These intensity fluctuations can be quantified by plotting their distribution functions, shown in figs. 5(c) and (d), where we plot the probability $P(\hat{I})$ of observing the different values of the intensity normalized by the mean, $\hat{I} = I/\langle I \rangle$. In the diffuse regime, $P(\hat{I})$ is close to the well-known Rayleigh distribution, $P(\hat{I}) = \exp(-\hat{I})$, for random wave fields described by circular Gaussian statistics, such as can be observed for light from a laser beam scattered off a rough, random surface. The small deviations seen for $P(\hat{I}) < 10^{-2}$ in fig. 5(c) can be explained by the leading order corrections to Rayleigh statistics calculated by Shnerb and Kaveh [33], and by Nieuwenhuizen and van Rossum [34]. Their expression, $P(\hat{I}) = \exp(\hat{I})[1 + (\hat{I}^2 - 4\hat{I} + 2)/3g]$, contains only one parameter, the dimensionless conductance g, and gives an excellent description of the experimental results, with $g = 11.4 \pm 0.8 >> 1$. By contrast, near 2.4 MHz in the localized regime (fig. 5(d)), the intensity distribution function exhibits huge departures from Rayleigh statistics, with greatly enhanced probability of observing large values of the normalized intensity, extending up to 50 times the average. To improve the accuracy of the measurements, $P(\hat{I})$ for the localized regime was determined from data for four equivalent samples over a range of 101 frequencies between 2.35 and 2.45 MHz. Figure 5(d) shows that the data can be extremely well fitted over the entire range of intensities by Nieuwenhuizen and van

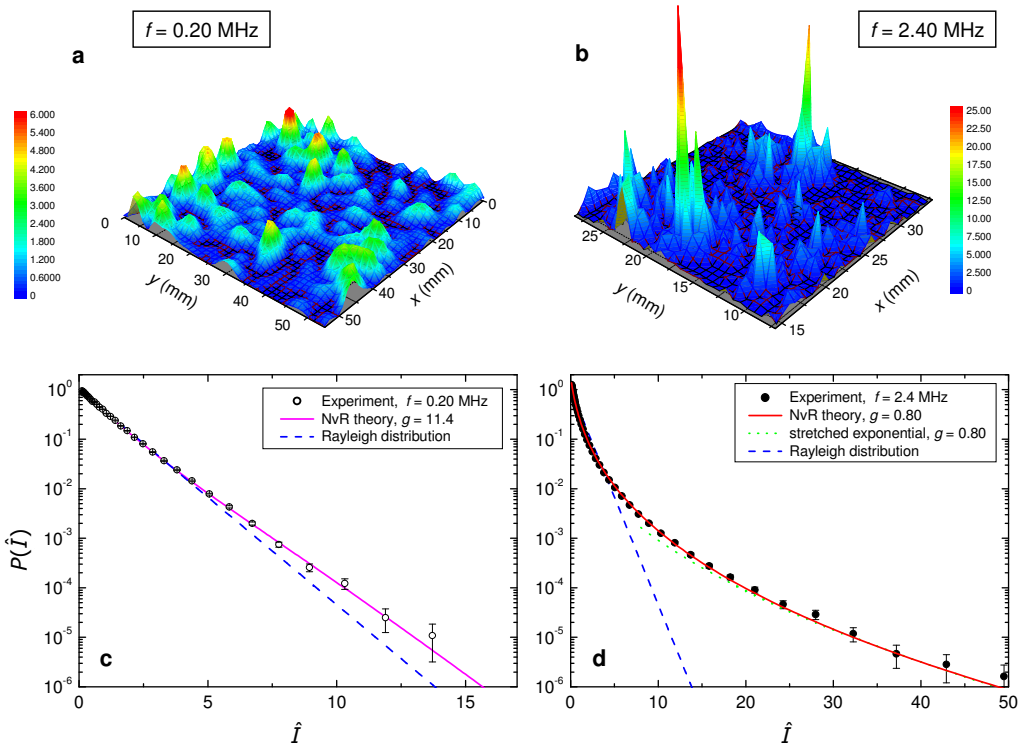

Fig. 5. – (a),(b): Comparison of the near field speckle patterns, showing the spatial variation of the intensity normalized by its average value, $I(x,y)/\langle I\rangle$, at frequencies of 0.20 (a) and 2.4 MHz (b). In (a), the speckle pattern is typical of the diffuse regime, with broad overlapping speckle spots, while in (b) the pattern is dominated by narrow intense peaks that are characteristic of Anderson localization. In these two figures, the colour scale is different, but the z-axis scale (perpendicular to the plane) is the same so that the striking differences in these speckle patterns can be readily seen. (c): The measured probability distribution $P(\hat{I})$ at 0.2 MHz (open circles) is close to the Rayleigh distribution (dashed blue line). The solid magenta curve is best fit of the theory of ref. [34] to the data with $g = 11.4$. (d): At 2.4 MHz, the probability of observing large intensities relative to the mean is very much greater than for diffuse waves. The solid curve shows the theory [34] for $P(\hat{I})$ with $g = 0.80$, and is in excellent agreement with the experimental data (solid symbols). At large $\hat{I} \gtrsim 25$, the data can also be described by a stretched exponential with the same value of g (dotted curve). The large deviation from Rayleigh statistics with $g < 1$ provides additional evidence that the Anderson localization of ultrasound has occurred at frequencies near 2.4 MHz. [Nature Physics, **4**, 945 (2008)]

Rossum's theory for $P(\hat{I})$, yielding a value of $g = 0.80 \pm 0.08$. The theoretical expressions used in the fits were determined for a broad Gaussian beam incident on a slab-shaped sample, and account for interference processes dominated by the loopless connected diagrams [34]. For large intensities, the data can also be fitted by a stretched exponential, $\exp(-2\sqrt{g\hat{I}})$, with the same value of g, a simple analytic form of $P(\hat{I})$ that can be de-

duced from the complete intensity distribution derived in ref. [34]. These observations of very large intensity fluctuations, for which the analysis of $P(\hat{I})$ reveals $g < 1$, provide additional evidence [6] that localization has occurred in our samples at high frequencies. This interpretation is consistent with the Thouless criterion that $g < 1$ implies localization. It is remarkable that such good agreement between theory and experiment for $P(\hat{I})$ has been found, as the theory was derived for the intensity in the far field and for $g > 1$; this excellent agreement suggests a universality of the statistics of localized waves.

A simple way of characterizing the intensity fluctuations is measuring the variance, $\langle \hat{I}^2 \rangle$. At 0.2 MHz, we find $\langle \hat{I}^2 \rangle = 1.12 \pm 0.02$, very close to the value of 1 for Rayleigh statistics, while at 2.4 MHz, a much larger value is found, $\langle \hat{I}^2 \rangle = 2.74 \pm 0.09$. The variance of the normalized speckle intensities can be directly related to the dimensionless conductance, $\langle \hat{I}^2 \rangle = 1 + 4/(3g)$ [6], providing an easier way of determining g. Using our measured values of $\langle \hat{I}^2 \rangle$, this relation gives $g = 11.5 \pm 2$ at 0.2 MHz, and $g = 0.77 \pm 0.04$ at 2.4 MHz, in good agreement with the values of g determined from fitting the intensity distributions. Note that the localization condition $g < 1$ implies that localization will be reached when the variance $\langle \hat{I}^2 \rangle > 7/3$ [6]. The measured variance at 2.4 MHz is larger than the threshold value 7/3, again supporting our conclusions that ultrasound is localized at this frequency.

The ability of these ultrasonic experiments to measure the wave functions very near the surface of a localized sample suggests that the spatial structure of localized wave functions can now be investigated experimentally. There is a large body of theoretical and numerical work that predicts that wave functions at the Anderson transition have multifractal character - a striking relation between the spatial structure of wave functions and their large fluctuations at criticality [35]. However, there have been virtually no experimental studies until very recently. The following paragraphs outline recent progress in using our ultrasonic data to examine this remarkable aspect of critical wave functions close to the Anderson transition [14].

Multifractality implies that the moments of the wave function intensity, $I(\vec{r}) = |\psi^2(\vec{r})| / \int |\psi^2(\vec{r})| d^d\vec{r}$ depend anomalously on length scale, with each moment scaling as a power law with a different exponent. Note that $I(\vec{r})$ is now normalized by the total intensity, rather than the average intensity, and is therefore normalized in the same way as $|\psi^2(\vec{r})|$ for quantum systems. To characterize this length scale dependence experimentally, one can either vary the size L of the samples, or, with a sample of a fixed size, divide the sample into boxes of linear size b, and vary b. The latter is easier to implement in practice, and is therefore used for our experimental data; it allows the size dependence to be expressed in terms of the dimensionless scaling length L_g/b, where L_g is the size of the speckle pattern over which the intensity is normalized. Note that in this analysis, since we can only measure the wave function on or near the surface of the sample, the dimension of the measurement space is $d = 2$, even though the sample is definitely three dimensional. This procedure is illustrated in fig. 6, which shows the transmitted intensity for three frequencies near 2.4 MHz for a point source. (The point source geometry has the advantage in this context of being more likely than an extended beam to excite a single wave function.)

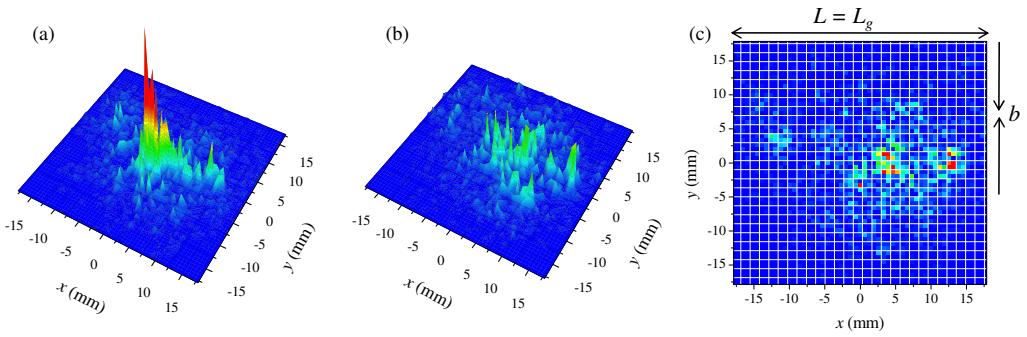

Fig. 6. – Speckle patterns at three representative frequencies near 2.4 MHz [(a) 2.35 MHz, (b) 2.375 MHz, and (c) 2.425 MHz] when a point source is incident on the opposite face of the sample. In (a) and (b), the speckle intensities very close to the sample surface are plotted as three-dimensional intensity maps, so that the large fluctuations with position are easy to see. In (c), a contour plot is shown to illustrate the box-counting method used to determine the system size dependence in terms of the dimensionless scaling parameter L_g/b. In this example, the box size b is 2.

The length scale dependence of the moments of the intensity is quantified by the generalized Inverse Participation Ratios (gIPR), which are defined as

$$P_q = \sum_{i=1}^{n} (I_{B_i})^q = \sum_{i=1}^{n} \left[\int_{B_i} I(\vec{r}) d^d\vec{r} \right]^q . \tag{6}$$

Here I_{B_i} is the integrated probability inside box B_i of linear size b, with $\lambda < b < L_g$, and the summation is performed over all of the $n = (L_g/b)^d$ boxes. By definition, $P_1 \equiv 1$ and $P_0 \equiv n$. The length scale dependence was studied experimentally experimentally by determining the "typically averaged" gIPR for a single realization of disorder. In the critical regime, the average gIPR are expected to scale anomalously with L_g/b as

$$\langle P_q \rangle \sim (L_g/b)^{-\tau(q)} \equiv (L_g/b)^{-d(q-1)-\Delta_q} , \tag{7}$$

where the exponent $\tau(q)$ is written in terms of the normal (Euclidean) dimension $d(q-1)$ and the anomalous dimension, Δ_q. Typical results for $\langle P_q \rangle$ from the ultrasonic data at 2.4 MHz are shown in fig. 7(a) for integer values of q between -2 and 3. By plotting the data on doubly logarithmic scales, power law behaviour is clearly seen over more than a decade in L_g/b, as shown by the excellent fits of the data to straight lines. The slopes of these linear fits yield $\tau(q)$, from which the anomalous exponents Δ_q were determined by subtracting off the normal part $d(q-1)$. Average values of the anomalous exponents were determined by averaging over many frequencies between 2.0 and 2.6 MHz.

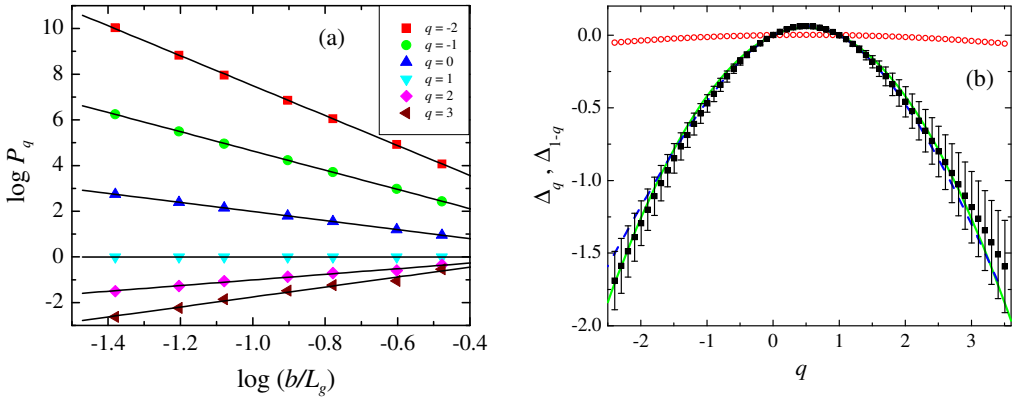

Fig. 7. – (a) An example of the dependence of the gIPR on box size at a frequency of 2.4 MHz, for integer values of q between -2 and 3. Box sizes of $b = 2, 3, 4, 68, 12$ and 24 were used. The grid size, L_g, was 55. (b) The anomalous exponents Δ_q measured for localized ultrasound (solid squares) and diffuse light (open circles). For the localized ultrasound exponents, the data mirrored relative to $q = 1/2$ are indicated by the dashed curve, showing the symmetry of the measured values of Δ_q. The solid curve is a fit to the parabolic approximation.

The q-dependence of the anomalous exponents is shown in fig. 7(b), where the results for localized ultrasonic wave functions are compared with data from an optical speckle pattern for diffuse waves. The behaviour seen for these two data sets is obviously very different. For the diffuse optical data, the open circles in this figure show that $\Delta_q \approx 0$, consistent with expectations for a normal (extended) wave function that $\Delta_q = 0$ for every q. By contrast, for multifractal wave functions, such as are expected in the critical regime of the Anderson transition, $\tau(q)$ and hence Δ_q are expected to be continuous functions of q, with substantial departures from Euclidean behaviour. This is precisely what fig. 7 shows for Δ_q determined from the ultrasonic data, clearly indicating that each intensity moment has a different fractal exponent. In other words, the q-dependence of Δ_q in fig. 7(b) reveals unambiguous evidence for multifractality of the localized ultrasound wave functions.

The ultrasonic data in fig. 7(b) enables a recently predicted symmetry relation for the anomalous exponents Δ_q to be tested experimentally. This relation, $\Delta_q = \Delta_{1-q}$, was predicted to hold exactly for multifractal wave functions at the Anderson transition [36]. The dashed blue curve in fig. 7(b) represents the experimental results reflected about $q = 1/2$, showing that this symmetry relation is consistent with our data. As the theoretical predictions of this symmetry relation were made in the context of particular symmetry classes of electronic systems, its observation in our ultrasonic experiments provides evidence for the universality of critical properties at the Anderson transition.

The solid curve in fig. 7(b) is a fit of the predictions of the parabolic approximation to our data. This analytic approximation, derived in first-order perturbation theory for an Anderson transition in $2 + \epsilon$ dimensions, gives the simple expression $\Delta_q = \gamma q(1 - q)$.

This expression describes the ultrasonic data well, with $\gamma = 0.21$. The parabolic approximation also gives simple analytic expressions for two other important measures of multifractality, the probability density function and the so-called singularity spectrum, both of which were also measured for our ultrasonic data, as reported in ref. [14]. The measurement of all three manifestations of multifractality, anomalous exponents, the (log-normal) probability density function and the singularity spectrum, have demonstrated an aspect of Anderson transitions that has not been studied experimentally before. This opens up a number of interesting questions for future work, such as seeking an understanding of why the value of γ for the ultrasonic data is smaller than predicted for the 3D Anderson tight-binding model [35], and exploring the relationship between multifractal properties and the critical exponents governing the Anderson transition [37].

6. – Conclusions

Ultrasonic experiments have several advantages for observing and studying Anderson localization. As for all classical waves, they benefit from the convenience and versatility that is associated with performing experiments at room temperature. More important is the ability to readily investigate not only average wave transport at a single frequency, but also the propagation of the multiply scattered wave fields resolved in time and space. This has enabled the development of a new approach, transverse confinement, that has permitted the most direct observation so far of Anderson localization in 3D, and provides a valuable method for guiding future investigations of localization for any type of wave. In particular, the measurement of the dynamic transverse confinement is a powerful way, which is not affected by absorption, for assessing whether or not waves are localized; it also enables the localization length to be measured.

By combining this approach with measurements of the time-dependent transmission and the statistics of the large non-Gaussian intensity fluctuations, recent ultrasound experiments, in conjunction with theoretical advances, have enabled the most unambiguous demonstration of 3D Anderson localization of classical waves to date. These results suggest that ultrasonic experiments on well controlled samples may be able to investigate previously unexplored aspects of 3D Anderson localization. One of these aspects, the characterization of the multifractal spatial structure of wave functions near the Anderson transition, has already been realized. It is reasonable to anticipate that an even more complete study of 3D Anderson localization using ultrasound is now within reach.

Appendix A.

Schrodinger and Helmholtz equations in disordered media

A quantum particle of energy E in a random potential $V(\vec{r})$is described by the wave function $\psi(r)\exp(-iEt/\hbar)$, where $\psi(\vec{r})$ obeys the time-independent Schrodinger equation

$$\left[-\frac{\hbar^2}{2m}\nabla^2 + V(\vec{r})\right]\psi(\vec{r}) = E\psi(\vec{r}). \tag{A.1}$$

A monochromatic scalar classical wave (e.g., sound, or light if one neglects polarization) with angular frequency ω obeys the Helmholtz equation

$$\left[\nabla^2 + \frac{\omega^2}{v^2}\right]\psi(\vec{r}) = 0, \tag{A.2}$$

where, for the example of acoustic waves, the wave function $\psi(\vec{r})$ corresponds to the pressure. In a disordered medium, the wave velocity $v(\vec{r})$ varies with position, and the Helmholtz equation can be rewritten in terms of the fluctuations of wave speed relative to the average speed v_0 as

$$\left[-\nabla^2 + \sigma\left(\vec{r}\right)\right]\ \psi(\vec{r}) = \frac{\omega^2}{v_0^2}\psi(\vec{r}) \tag{A.3}$$

Here $\sigma(\vec{r}) = \omega^2/v_0^2 - \omega^2/v^2(\vec{r})$. This equation has the same form is the Schrodinger equation if one considers $\sigma(\vec{r})$ to play the role of an effective potential (the analogue of $2mV(\vec{r})/\hbar^2$), and ω^2/v_0^2 to play the role of an effective energy (the analogue of $2mE/\hbar^2$). This analogy indicates that similar wave phenomena can be expected for quantum particles and classical waves. However, there is an important difference. Since $\sigma(\vec{r}) > \omega^2/v_0^2$ always, the classical wave case corresponds to the quantum case *only* when $E > V(\vec{r})$ for all $\vec{r}$. Thus classical waves can never be trapped by disorder in a trivial way analogous to the trapping of a low-energy particle in the bottom of a potential well. For classical waves, lowering the frequency also lowers the effective disorder potential seen by the wave, since $\sigma(\vec{r})$ is proportional to ω^2, so that localization is most likely to occur at intermediate frequencies where the wavelength is comparable with the size of the inhomogeneities and the scattering is greatest.

* * *

I would like to acknowledge the theoretical contributions made by Sergey Skipetrov and Bart van Tiggelen to the work reviewed in this paper, and to Sanli Faez for suggesting and carrying out the multifractal analysis. None of this research would have been possible without the hard work of Hefei Hu and Anatoliy Strybulevych in my research group at the University of Manitoba, who made the samples and performed the ultrasonic experiments. Support from NSERC and a CNRS PICS grant is also gratefully acknowledged.

REFERENCES

[1] ANDERSON P.W., *Phys. Rev.*, **109** (1958) 1492.

[2] For a recent non-specialist review of Anderson Localization, see Lagendijk A., van Tiggelen B.A. and Wiersma D.S., *Physics Today*, **62(8)** (2009) 24.
[3] He H. and Maynard J.D., *Phys. Rev. Lett.*, **57** (1986) 3171.
[4] Weaver R.L., *Wave Motion*, **12** (1990) 129.
[5] Dalichaouch R., Armstrong J.P., Schultz S., Platzman P.M. and McCall S.L., *Nature*, **354** (1991) 53.
[6] Chabanov A.A., Stoytchev M. and Genack A.Z., *Nature*, **404** (2000) 850.
[7] Chabanov A.A., Zhang Z.Q. and Genack A.Z., *Phys. Rev. Lett.*, **90** (2003) 203903.
[8] Schwartz T., Bartal G., Fishman S. and Segev M., *Nature*, **446** (2007) 52.
[9] Wiersma D.S., Bartolini P., Lagendijk A. and Righini R., *Nature*, (390,) 671–673 (1997).
[10] Störzer M., Gross P., Aegerter C.M. and Maret G., *Phys. Rev. Lett.*, **96** (2006) 063904.
[11] Aegerter C.M., Störzer M. and Maret G., *Europhys. Lett.*, **75** (2006) 562.
[12] Abrahams E., Anderson P.W., Licciardello D.C. and Ramakrishnan T.V., *Phys. Rev. Lett.*, **42** (1979) 673.
[13] Hu H., Strybulevych A., Page J.H., Skipetrov S.E. and van Tiggelen B.A., *Nature Physics*, **4** (2008) 945
[14] Faez S., Strybulevych A., Page J.H., Lagendijk A. and van Tiggelen B.A., *Phys. Rev. Lett.*, **103** (2009) 155703
[15] Page J.H., this volume, p. 75.
[16] Page J.H., Hildebrand W.K., Beck J., Holmes R. and Bobowski J., *Phys. Stat. Sol. (c)*, **1** (2004) 2925.
[17] Page J.H., Schriemer H.P., Bailey A.E. and Weitz D.A., *Phys. Rev. E*, **52** (1995) 3106.
[18] Turner J.A., Chambers M.E. and Weaver R.L., *Acustica*, **84** (1998) 628.
[19] Schriemer H.P., Pachet N.G. and Page J.H., *Waves in Random Media*, **6** (1996) 361.
[20] Van Tiggelen B.A., in *Diffuse Waves in Complex Media*, edited by Fouque, J.P. (Dordrecht, Kluwer, 1998), pp. 1-63.
[21] Weaver R.L., *J. Acoust. Soc. Amer.*, **71** (1982) 1609.
[22] Ryzhik L., Papanicolaou G. and Keller J.B., *Wave Motion*, **24** (1996) 327.
[23] Hennino R., Trégourès N., N. M. Shapiro N.M., Margerin L., Campillo M., van Tiggelen B.A., and Weaver R.L., *Phys. Rev. Lett.*, **86** (2001) 3447.
[24] Turner J.A. and Weaver R.L., *J. Acoust. Soc. Amer.*, **98** (1995) 2801.
[25] Vollhardt D. and Wölfle P., *Phys. Rev. B*, **22** (1980) 4666; *Phys. Rev. Lett.*, **48** (1982) 699.
[26] Wölfle P., this volume, p. 1.
[27] van Tiggelen B.A., Lagendijk A. and Wiersma D.S., *Phys. Rev. Lett.*, **84** (2000) 4333.
[28] Skipetrov S.E. and van Tiggelen B.A., *Phys. Rev. Lett.*, **96** (2006) 043902.
[29] Indeed, if one were to use the solutions of the standard diffusion equation assuming only that the diffusion coefficient varies with time, serious inconsistencies are found when comparing $D(t)$ extracted by this approach for planar and point source geometries, yielding results for $D(t)$ differing by two orders of magnitude [30]. This comparison provides another indication of the inadequacy of this approach for our data.
[30] Hu H.,, Ph.D. Thesis, University of Manitoba, 2006.
[31] Cherroret N., Skipetrov S.E. and van Tiggelen B.A., arXiv:0810.0767.
[32] Scheffold F., Lenke R., Tweer R. and Maret G., *Nature*, **398** (1999) 206.
[33] Shnerb N. and Kaveh M., *Phys. Rev. B*, **43** (1991) 1279.
[34] Nieuwenhuizen Th.M. and van Rossum M.C.W., *Phys. Rev. Lett.*, **74** (1995) 2674; van Rossum M.C.W. and Nieuwenhuizen Th.M., *Rev. Mod Phys.*, **71** (1999) 313.

[35] For a recent review, see Evers F. and Mirlin A.D., *Rev. Mod. Phys.*, **80** (2008) 1355.
[36] Mirlin A.D., Fyodorov Y.V., Mildenberger A., and Evers F., *Phys. Rev. Lett.*, **97** (2006) 046803.
[37] Grussbach H. and Schreiber M., *Phys. Rev. B*, **51** (1995) 663.